

# Optimal Primary Coil Size for Wireless Power Telemetry to Medical Implants

Shawn K. Kelly, Patrick Doyle, Attila Priplata  
Center for Innovative Visual Rehabilitation  
VA Boston Healthcare System  
Boston, MA, USA  
skkelly@alum.mit.edu

Oscar Mendoza, John L. Wyatt  
Research Laboratory of Electronics  
Massachusetts Institute of Technology  
Cambridge, MA, USA

**Abstract**—A retinal prosthesis telemetry system is examined, and several methods are explored to optimize the size of the external primary telemetry coil to maximize the wireless delivery of power to an implanted secondary coil of constrained size. A simplified version of the Biot-Savart Law is used to give a first-pass optimal primary coil size for a small secondary coil. Numerical integration is then used to improve the optimization for larger secondary coils, and this calculation is repeated across a range of secondary coil radii. Finally, the effects of eye rotation angle are explored, with the future goal of expanding the optimization techniques to cover the predicted range of angular eye excursions.

**Keywords**-retinal prosthesis; retinal implant; telemetry; neural stimulation; biomedical engineering

## I. INTRODUCTION

Implanted active medical devices are used for neural and muscular tissue stimulation in a variety of applications, such as cochlear implants, cardiac pacemakers, and retinal prostheses [1]–[11]. Most cochlear and retinal prostheses receive power wirelessly, via an inductive telemetry link, from a battery outside the body [12]. Our retinal prosthesis will include an external camera mounted on a pair of glasses, connected to a small controller and battery pack that together are slightly larger than a mobile cellular phone. The glasses will also house a primary coil, which will be inductively coupled to a secondary coil on the eye that is connected to the implanted electronics. This inductive link will be used to transmit power and image data to the implant and status data from the implant (Fig. 1). We wish to deliver enough power to operate our retinal prosthesis while minimizing the magnetic field levels to which the patient is exposed. Put another way, we wish to maximize collected magnetic field at the secondary coil for a given field generated by the primary coil.

Our current retinal prosthesis prototype [3] uses a secondary telemetry coil that is implanted on the front of the eye, surrounding the cornea, under the conjunctiva. Because of its location, this coil is very constrained in its shape and size, so the mutual inductive coupling between the primary and secondary coils can only be optimized by varying the size of the primary coil. This paper examines the optimal choice of primary coil size with varying degrees of detail and with

This work was supported in part by the VA Boston Healthcare System, Center for Innovative Visual Rehabilitation, NIH (EY016674-01), and the Catalyst Foundation.

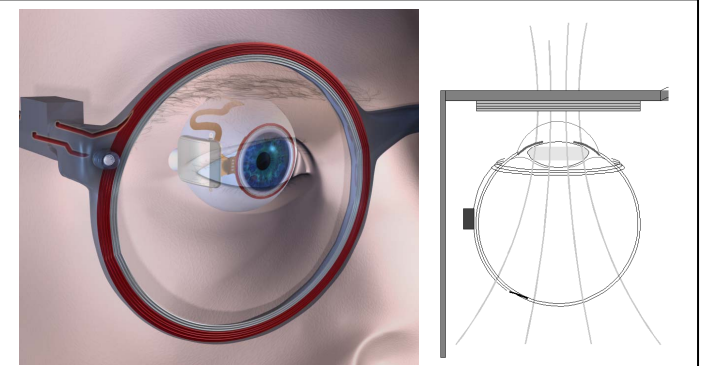


Figure 1. Retinal implant concept. Glasses worn by the patient carry a camera which collects image data. A controller unit with integrated battery pack (not shown) processes the image, then sends image data and power from the battery to the implant wirelessly via inductive coupling. The primary coil is embedded in the patient's glasses and the secondary coil is surgically inserted onto the eye, under the conjunctiva.

various methods, and makes an initial exploration into the effects of eye rotation on inductive coupling.

## II. BACKGROUND ON INDUCTIVE COUPLING

Delivering sinusoidal alternating current to a coil of wire creates a sinusoidal magnetic field in space. The magnitude of that peak  $\phi$ -directed field,  $d\bar{H}$ , passing through any point distance  $r$  from the primary coil, forming angle  $\theta$  with a small piece of primary coil wire of length  $ds$  carrying current  $I$  is expressed by the Biot-Savart Law:

$$d\bar{H} = \frac{1}{4\pi} \frac{Id\vec{s} \times \hat{r}}{r^2} = \frac{1}{4\pi} \frac{Ids \sin \theta}{r^2} \hat{\phi} \quad (1)$$

This expression is not easy to solve symbolically, but it is simple to solve for the field down the axis between the primary and secondary coils. The peak magnetic field,  $H$ , at the center of a secondary coil at axial displacement  $z$  from a primary coil of radius  $r_p$  and with  $N_p$  turns, carrying current with peak amplitude  $I_p$ , is plotted in Fig. 2, and is:

$$H = \frac{N_p I_p}{2} \frac{r_p^2}{(r_p^2 + z^2)^{\frac{3}{2}}} \quad (2)$$

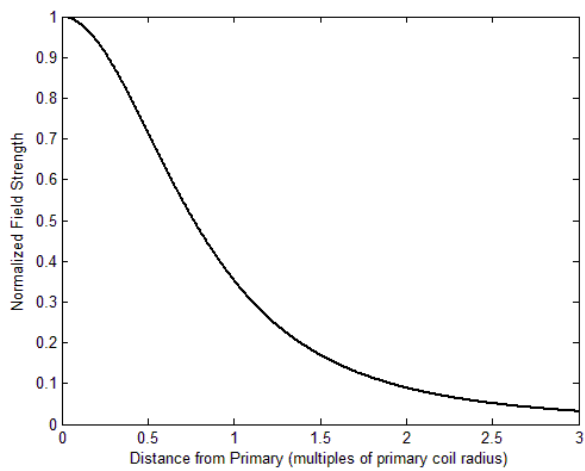


Figure 2. Plot of normalized magnetic field vs. normalized displacement. If the secondary is located one primary coil radius away from the primary, the field at the secondary has already dropped to 35% of the field at the center of the primary.

We can find a maximum for  $H$  by differentiating (2) with respect to  $r_p$  and setting the result equal to zero, which results in:

$$r_p = \sqrt{2}z. \quad (3)$$

This simple result is a handy equation for finding a first-order optimal size for a primary coil. It works well if the secondary coil is small compared to the primary coil and to the displacement. However, if the secondary coil is not very small, as in the case of our implant, numerical integration should be used to reduce errors. In addition, if the secondary coil is expected to move or rotate, as it will on a rotating eye, the choice of primary coil size should serve to limit the effect of the rotation on power delivered to the implant.

### III. METHODS

#### A. Exact Field Integration

The Biot-Savart Law (1) is numerically integrated across a secondary coil using a script for MATLAB (The MathWorks, Natick, MA, USA) written by the authors and provided in the appendix of [13]. For each small segment of primary coil, the script integrates the normal portion of the resulting field across the area of the secondary coil. Fig. 3 shows the definitions used in this integration.

The first step is to integrate the Biot-Savart expression across a secondary coil to determine the error from using the central field approximation in (2). This is the calculation performed in [13], and is performed here with a secondary coil radius of 9.75 mm, primary coil radius of 18.5 mm, and displacement between coils of 15 mm. The data are displayed in Fig. 5 in the Results section.

The more interesting calculation uses the numerical field integration calculator to find the primary coil size that maximizes the integrated field strength at the secondary. For

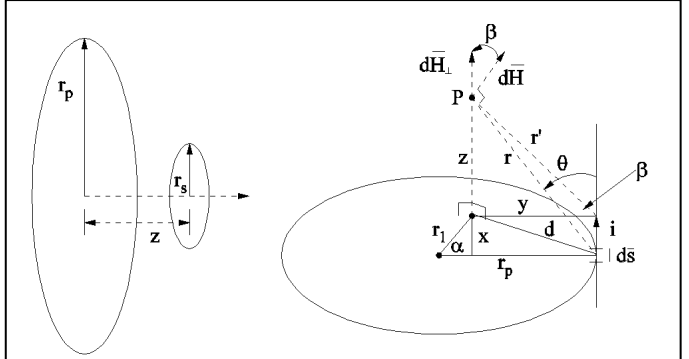


Figure 3. Definition of terms in the numerical integration script. On the left are the primary and secondary coils, coaxially aligned at distance  $z$ . On the right, the primary coil has been rotated, and the field at point  $P$  is shown. The field,  $d\mathbf{H}$ , is normal to the vector  $\mathbf{r}$  between the piece of secondary coil,  $ds$ , and point  $P$ . The component of the field that is normal to the secondary coil area,  $d\mathbf{H}_\perp$ , is used for the integration.

this calculation, we assumed a secondary coil with a radius of 9.75 mm, and a displacement between primary and secondary coils of 15 mm. Knowing that the optimal primary coil radius is roughly 1.414 times the displacement, or 21.2 mm, we created a vector of primary coil radii from 18 mm to 27 mm. For each primary coil radius, we integrated the field at every point on the secondary from each point around the primary, then found the mean field throughout the secondary coil. We created a vector of mean values, corresponding to the vector of primary coil radii, and found the maximum mean field and optimal primary coil radius. These data are plotted against field values along the axis from (2) in Fig. 6 in the Results section.

Another useful calculation is finding optimal primary coil sizes for an array of secondary coil sizes at a fixed displacement. We again chose 15 mm as the displacement, but varied the secondary coil radius from nearly zero (15  $\mu\text{m}$ ) to ten times the displacement (150 mm). As before, we created a vector of primary coil radii, and calculated mean integrated field values across the secondary for each primary radius. We repeated these calculations for each secondary coil radius. These data are presented in Fig. 7 in the Results section.

#### B. Angular Displacement Measurements

To learn more about the effects of eye movement on inductive coupling, we have created a non-conductive plastic test jig for measuring coupling between coils [13], and affixed to it a rotating arm with a radius of 12 mm, the approximate radius of the human eye (Fig. 4). Our secondary coil is affixed to this arm. This secondary coil (Precision Econowind, N. Fort Myers, FL, USA) is the same as that used in our implant [3]. It is wound on a spherical mandrel to better fit the shape of the eye, and is designed to be very low-profile to minimize irritation to the conjunctiva. It contains 74 turns of AWG 44 copper wire (to be replaced with gold wire in human implants), and has a mean radius of 9.75 mm and an inductance of 240  $\mu\text{H}$ . Our primary coil for this experiment is 10 turns of AWG 28 copper wire wrapped around a plastic form, with a radius of 22.5 mm and an inductance of 9.66  $\mu\text{H}$ .

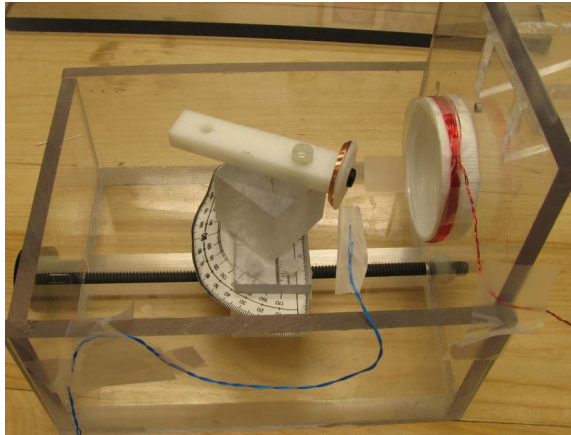


Figure 4. Non-conductive test jig for magnetic field experiments. The frame is made of polycarbonate and moving parts are made of nylon or delrin so that the jig does not interfere with magnetic fields. The secondary coil is attached to a rotating arm, with a radius approximating that of the human eye.

A sinusoidal voltage was applied to the primary coil with an Agilent 33250A function generator with a  $50 \Omega$  output resistance, at voltages of 0.8, 1, and 1.2 V, and at frequencies of 400, 500, and 600 KHz. The resulting voltage on the secondary coil was viewed on a Tektronix TDS3054b oscilloscope and was recorded. The angle of the secondary coil was swept from 0 to 60 degrees from the axis of the primary coil, measured from a crude protractor built into the test jig (Fig. 4). The data collected were primary coil voltage inputs and secondary coil voltage outputs, and we wanted to plot a normalized version of mean secondary coil magnetic field per ampere of primary coil current. We calculated the primary coil input current as the input voltage divided by the input impedance, which was the sum of the coil impedance ( $2\pi f L$ ) and the function generator output impedance ( $50 \Omega$ ). The open-circuit voltage for a secondary coil of  $N_s$  turns and cross-sectional area  $A_s$ , exposed to mean magnetic field  $H$ , is:

$$V_o = \frac{d\lambda}{dt} = N_s \omega A_s H \mu_0. \quad (4)$$

The mean field, then, is proportional to the open-circuit voltage divided by  $\omega$ . We used this value, proportional to the magnetic field, divided by the input current, and divided all of the resulting values by the highest value to normalize. These normalized data are plotted in Fig. 8 in the Results section.

#### IV. RESULTS AND DISCUSSION

##### A. Field Integration Data

The exact magnetic field values, numerically integrated from every point on the primary coil, are shown in Fig. 5 for every radial point on the secondary coil. For the coil radii and displacement used in this calculation (typical values for our implant), the field at the edge of the secondary is 89% of the field at the center, and the mean field is 95% of that at the center. This is not an enormous error, but can affect our choice of optimal primary coil size.

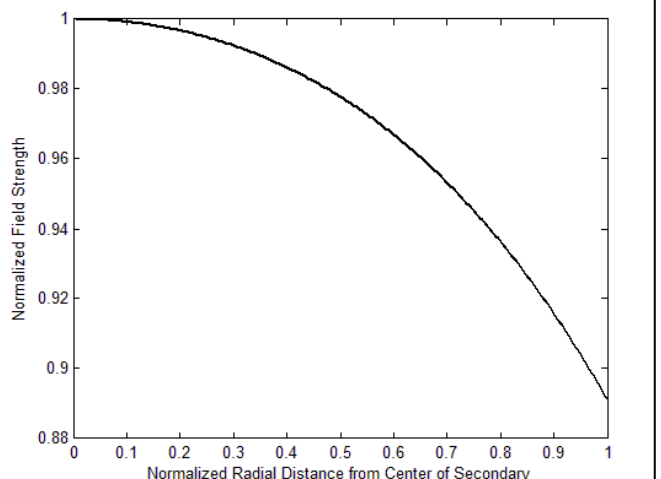


Figure 5. Normalized magnetic field vs. radial distance along the secondary coil. For the coil radii and displacement used here, the field at the edge of the secondary coil is 89% of that at the center.

The field strengths calculated by varying the primary coil radius are shown in Fig. 6. The dashed red line shows the mean value across the secondary coil area of the numerically-integrated magnetic field generated by primary coils of varying radius. The solid blue line shows the axial field, from (2), at the center of the secondary coil. Since the maxima occur at different locations on the plot, these two methods give two different optimal primary coil radii, as shown in the figure. The axial field approximation gives an optimal primary radius of 21.2 mm, as predicted by (3), but the more accurate numerical integration method shows that the optimal primary coil radius is 23.4 mm, meaning the axial approximation gives a 10% error in predicting the optimal coil size.

Repeating this calculation for a variety of secondary coil radii, we obtain the data shown in Fig. 7. We would expect the field across the very small secondary coil (15  $\mu\text{m}$ ) to be nearly equal to the field along the axis, and therefore the optimal

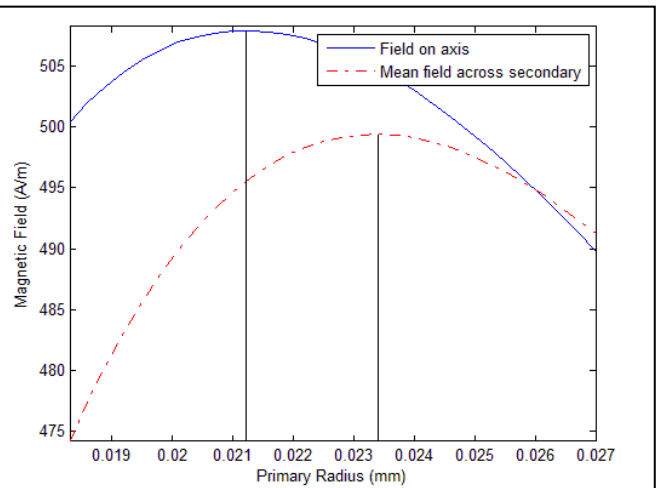


Figure 6. Magnetic field vs. primary coil diameter for the axial field and the mean numerically-integrated field. The maximum value for each is marked by a vertical line, showing different optimal primary coil radii.

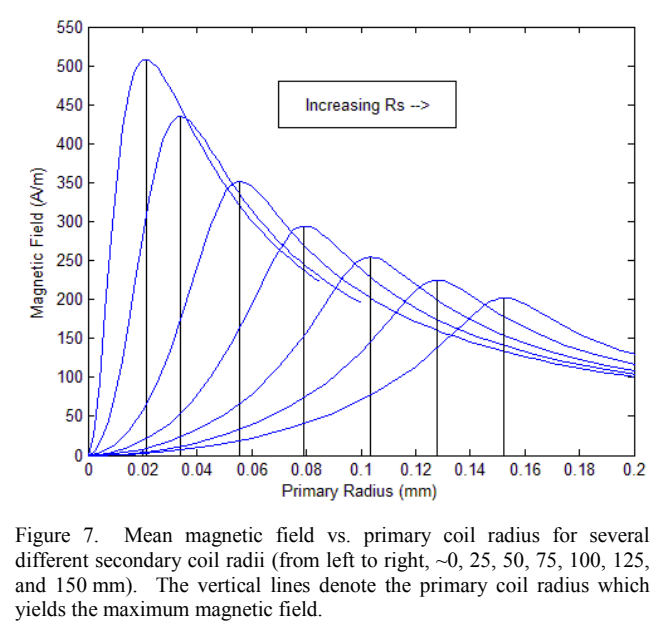


Figure 7. Mean magnetic field vs. primary coil radius for several different secondary coil radii (from left to right,  $\sim 0, 25, 50, 75, 100, 125$ , and  $150$  mm). The vertical lines denote the primary coil radius which yields the maximum magnetic field.

primary coil radius should be 21.2 mm, as predicted by (3) and as shown in the leftmost vertical line. As the secondary coil radius becomes much larger than the displacement, however, the telemetry coils begin to look like nearly concentric coils with no separation, and the size of the optimal primary coil approaches the size of the secondary coil. For example, as shown by the rightmost vertical line, the optimal primary coil to drive a 150 mm radius secondary at a displacement of 15 mm has a radius of 152.4 mm, almost identical to that of the secondary.

### B. Angular Displacement Data

The data showing normalized coupled field per ampere of input current are plotted in Fig. 8. Blue data represent transmissions at 500 KHz, red lines marked with “o” represent transmissions at 400 KHz, and green lines marked with “x” represent transmissions at 600 KHz. Solid lines represent input drive voltages of 1 V, while dotted blue lines represent 0.8 V and alternating dot-dash blue lines represent 1.2 V. While the secondary coil was rotated up to an angle of  $60^\circ$ , the maximum possible angle of left or right deflection for the human eye is  $50^\circ$  [14], and the maximum left or right deflections during normal use are  $35^\circ$ . Maximum up or down deflections under normal use are  $25^\circ$  and  $30^\circ$ , respectively, and a normal deflection in any direction is  $15^\circ$  [15].

As expected, the total field coupled by the secondary coil drops drastically with increasing angular displacement. Some of this is the effect of rotation and some is the effect of displacement off of the axis of the primary coil and displacement farther away from the primary. A cosine function is plotted as a dotted magenta line for reference, representing the purely rotational component of the drop in field with increasing angle. In a clinical implant, we expect the impact of this reduction in coupled field to be relatively minor under normal circumstances with  $15^\circ$  angular displacement.

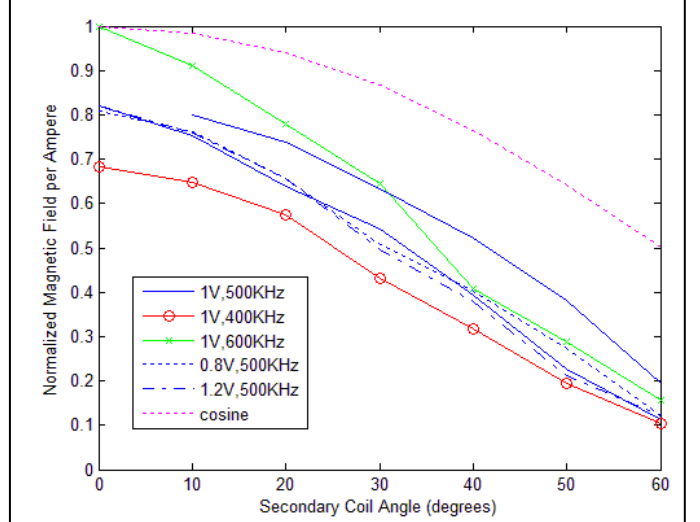


Figure 8. Normalized magnetic field coupled by the secondary coil per ampere of primary coil input current, plotted against the angle of the secondary coil. The dotted magenta line shows a cosine function for reference.

## V. CONCLUSIONS AND FUTURE WORK

We have presented a number of methods for choosing a primary coil size that will maximize the total magnetic field coupled by the secondary coil of a wirelessly-powered medical implant, in our application a retinal prosthesis. We have shown the simple case of the field down the center axis of the primary coil. Assuming the field everywhere on the secondary coil is the same as the axial field, the optimal primary coil size can be solved explicitly in this case. But we have also shown by numerical integration that the magnetic field will generally be smaller at points farther from the axis on the secondary coil, and that this can result in an error in optimal primary coil size of 10% in the case of our coil sizes and separation. We also re-calculated the optimal primary coil size for a wide variety of secondary coil sizes, showing the transition from the central axis field optimization to a case of nearly concentric telemetry coils. Finally, we explored the effect of angular rotation of the secondary coil on a 12 mm radius to simulate eye movement. While the total field collected by the secondary will drop, the effect should not be insurmountable in a clinical implant with normal angular eye movement. All of these optimizations will maximize the power received by the implant for a given magnetic field generated by the primary coil, allowing us to power a retinal prosthesis while minimizing the magnetic field exposure of the patient.

We will continue work on this topic, using the numerical integration tool created by the authors to predict magnetic coupling coefficients for telemetry coils. We will take measurements of coupling with a variety of primary and secondary coil sizes to verify the numerical data. We also plan to further explore the effects of angular displacement, trying to separate the effects of simple rotation from the effects of displacement off the primary coil axis, and displacement away from the primary coil. We will also predict the reduction in total power coupled to an implant under typical eye rotation

angles. Finally, we hope to further optimize the primary coil size to create a telemetry system that is more tolerant of normal eye rotation.

#### ACKNOWLEDGMENT

The authors acknowledge technical and scientific contributions of M. Markova, L. Theogarajan, M. Baker, R. Sarpeshkar, and J. F. Rizzo, as well as administrative support from J. Balzer, S. Davco, J. Dumser, and G. Galanek. We also acknowledge the cooperation and patience of T. Tingley of Precision Econowind.

#### REFERENCES

- [1] B. Ziaie, M. D. Nardin, A. R. Coghlan, and K. Najafi, "A single-channel implantable microstimulator for functional neuromuscular stimulation," *IEEE Trans. Biomed. Eng.*, vol. 44, no. 10, pp. 909-920, Oct. 1997.
- [2] D. B. Shire, et al., "Development and implantation of a minimally-invasive, wireless sub-retinal neurostimulator," *IEEE Trans. Biomed. Eng.*, 56: 10, pp. 2502-2511, 2009.
- [3] S. K. Kelly, et al., "The Boston retinal prosthesis: A 15-channel hermetic wireless neural stimulator," *IEEE ISABEL Int'l Symposium on Applied Sciences in Biomedical and Communication Tech.*, 2009.
- [4] D. Yanai, et al., "Visual performance using a retinal prosthesis in three subjects with retinitis pigmentosa," *Am. J. Ophthalmol.*, vol. 143, pp. 820-827, 2007.
- [5] H. Gerdin, F. P. Benner, and S. Taneri, "Experimental implantation of epiretinal retina implants (EPI-RET) with an IOL-type receiver unit," *J. Neural Eng.*, vol. 4, pp. S38-S49, 2007.
- [6] P. J. DeMarco, et al., "Stimulation via a subretinally placed prosthetic elicits central activity and induces a trophic effect on visual responses," *Invest. Ophthalmol. Vis. Sci.*, vol. 48, pp. 916-926, 2007.
- [7] T. Schanze, H. G. Sachs, C. Wiesenack, U. Brunner, and H. Sailer, "Implantation and testing of subretinal film electrodes in domestic pigs," *Exp. Eye Res.*, vol. 82, pp. 332-340, 2006.
- [8] J. A. Zhou, et al., "A suprachoroidal electrical retinal stimulator design for long-term animal experiments and in-vivo assessment of its feasibility and biocompatibility in rabbits," *J. Biomed. Biotech.*, vol. 2008, Article ID 547428, 10 pp., 2008.
- [9] Y. Terasawa, et al., "The development of a multichannel electrode array for retinal prostheses," *J. Artif. Organs*, vol. 9, pp. 263-266, 2006.
- [10] R. Hornig, et al., "The IMI retinal implant system," in M. S. Humayun, J. D. Weiland, G. Chader, and E. Greenbaum, eds., *Artificial Sight: Basic Research, Biomedical Engineering, and Clinical Advances*, New York: Springer, pp. 111-128, 2007.
- [11] E. Zrenner, "Restoring neuroretinal function: New potentials," *Doc. Ophthalmol.*, vol. 115, pp. 56-59, 2007.Y. Yorozi, M. Hirano, K. Oka, and Y. Tagawa, "Electron spectroscopy studies on magneto-optical media and plastic substrate interface," *IEEE Transl. J. Magn. Japan*, vol. 2, pp. 740-741, August 1987 [Digests 9th Annual Conf. Magnetics Japan, p. 301, 1982].
- [12] M. W. Baker, R. Sarpeshkar, "Feedback analysis and design of RF power links for low-power bionic systems," *IEEE Trans. Biomed. Circ. And Sys.*, vol. 1, no. 1, pp. 28-38, 2007.
- [13] S. K. Kelly, "A system for efficient neural stimulation with energy recovery," Ph.D. dissertation, Dept. Elect. Eng. and Comp. Sci., MIT, Cambridge, MA, 2004.
- [14] D. S. Childress, R. W. Jones, "Mechanics of horizontal movement of the human eye," *J. Physiol.*, 188(2), pp. 273-284, 1967.
- [15] Nelson and Associates, (2010, Sept.), "Human vision during the walking process," [website] Available: <http://www.hazardcontrol.com/print.php?fs=humanfactors&p=visual-acuity-and-line-of-sight>